Atomization Mechanism of Internally Mixing Twin-Fluid Y-Jet Atomizer

Y. H. Nazeer[1*], M. Ehmann[1], M. Sami[2], M. Gavaises[3]

[1]Mitsubishi Hitachi Power Systems Europe GmbH, Germany
[2]ANSYS, Inc., Houston, Texas, USA
[3]School of Mathematics, Computer Sciences and Engineering, City, University of London, UK

Abstract

The atomization mechanism of the gas-liquid multiphase flow through internally mixing twin-fluid Y-jet atomizer has been studied by examining both the internal and external flow patterns. Super-heated steam and Light Fuel Oil (LFO) are used as working fluids. The flow is numerically modeled using the compressible Navier-Stokes equations; hybrid Large Eddy Simulation approach through Wall Modeled Large Eddy Simulations (WMLES) is used to resolve the turbulence with the Large Eddy Simulations, whereas the Prandtl Mixing Length Model is used for modeling the subgrid-scale structures, which are affected by operational parameters. VOF-to-DPM transition mechanism is utilized along with dynamic solution-adaptive mesh refinement to predict the initial development and fragmentation of the gas-liquid interface through Volume-of-Fluid (VOF) formulations on a sufficiently fine mesh, while Discrete Phase Model (DPM) is used to predict the dispersed part of the spray on the coarser grid. Two operational parameters, namely gas-to-liquid mass flow rate ratio (GLR) and liquid-to-gas momentum ratio are compared; the latter is found to be an appropriate operational parameter to describe both the internal flow and atomization characteristics. It is confirmed that the variation in the flow patterns within the mixing-port of the atomizer coincides with the variation of the spatial distribution of the spray drops.

Keywords: Internally Mixing Twin-Fluid Y-Jet Atomizer, VOF-to-DPM, Wall Modeled Large Eddy Simulations (WMLES)

Nomenclature

Acronyms

SMD	Sauter Mean Diameter
VOF	Volume of Fluid
HPC	High-Performance Computing
WMLES	Wall Modeled Large Eddy Simulations
LES	Large Eddy Simulations
RANS	Reynolds-Averaged Navier-Stokes
DPM	Discrete Phase Model
SGS	Subgrid Scale
Eq.	Equation
HPC	High Performance Computing

Subscripts

p	Phase p
q	Phase q
m	Mixing Port
M	Mixing Point
g	Gas
l	Liquid
pz	Premix Zone
r	relative
pr	Particle
max	Maximum

min	Minimum
Superscript	
T	Transpose
s	Sub-grid Scale
Symbols	
α	Volume Fraction
ρ	Density, kg/m^3
V	Velocity, m/s
P	Pressure, Pa
μ	Viscosity, $kg/m.s$
g	Gravitational Acceleration, m/s^2
T_σ	Surface Tension Force, N
T	Temperature, K
k	Curvature, m^{-1}
σ	Surface Tension, N/m
E	Energy, J
K_∞	Thermal Conductivity, $W/m.K$
K_{eff}	Effective Thermal Conductivity, $W/m.K$
Δ	Modified Length Scale, m
τ_{ij}	Viscous Stress, N/m^2
ν_t	Eddy Viscosity, m^2/s
δ_{ij}	Kronecker Delta
y^+	Dimensionless Wall Distance
Ω	Vorticity, s^{-1}

S	Strain Rate, s^{-1}
θ	Angle, °
l	Length, mm
d	Diameter, m
τ_{kk}	Isotropic Part of the Subgrid Stress, N/m^2
φ	Momentum Ratio
M	Mass Flow Rate, kg/s
G	Mass Velocity, kg/m^2s
C_w	Empirical Constant
h_{max}	Maximum Edge Length, m
h_{wn}	Grid Step in Wall Normal Direction, m
d_w	Distance from Wall, m
C_{smag}	Smagorinsky Constant
a_1	Constant defined in Eq. 11
a_2	Constant defined in Eq. 11
a_3	Constant defined in Eq. 11
C_D	Drag Coefficient
F_D	Drag Force Per Unit Mass, N/kg
Ar	Surface Area, m^2
h	Convective Heat Transfer Coefficient, W/Km^2
Y	Coordinate Axis
C	Heat Capacity, J/K

26

27

28

Introduction

The description of “twin-fluid atomizer” can be applied to any nozzle in which the driving force for the liquid jet break up is air, steam or any gas. Twin-fluid atomizers could be classified into “air-assist,” “airblast” and “effervescent” atomizers (Lefebrve, 1992). One thing common between different types of twin-fluid air-assist atomizers (Mlkvik, et al., 2015), (Pacifico & Yanagihara, 2014) and (Kufferath, et al., 1999) and airblast atomizers (Inamura, et al., 2019), (Okabe, et al., 2019) and (Roudini & Wozniak, 2018) is that the bulk liquid to be atomized is first transformed into a jet or sheet before being exposed to high-velocity gas. In contrast, in effervescent atomizers (Roesler & Lefebvre, 1989), (Buckner, et al., 1990a), (Buckner, et al., 1990b) and (Sovani, et al., 2001) the atomizing gas is injected into the bulk liquid at low velocity to form a bubbly two-phase mixture upstream of the discharge orifice. The main difference between the air-assist and airblast atomizers is that the former employs high pressure source of air or steam at very high velocities (usually sonic) and at relatively smaller mass flow rates while the latter employ low pressure gas source and much larger amount of gas flow at relatively lower velocities (Lefebrve, 1992) and (Lefebvre, 1980).

Air-assist atomizers can be classified into internal-mixing and external-mixing types. In the former, high velocity air or steam impinges on the liquid jet within the mixing chamber of the nozzle while in the latter the air or steam impinges on the liquid sheet or jet outside the discharge orifice. In the external mixing type, the spray cone angle is minimum for the maximum gas flow, and the spray widens as the gas flow is reduced; whereas external mixing type can be designed to give constant spray angle at all liquid flow rates. Internal mixing air-assist atomizers are highly suitable for high viscous liquids, as good atomization can be achieved down to very low liquid mass flow rates (Barreras, et al., 2008).

In large oil-fired industrial boilers or thermal power plants, either Y-jet atomizers or internal mixing chamber twin-fluid atomizers are used (Barreras, et al., 2006). The former is usually used with light fuel oil while the latter is used with heavy fuel oil and steam as auxiliary fluid (Li, et al., 2012). The

characteristics of the Y-jet atomizer is that the liquid and gas (air or steam) are mixed before injected out. It generally consists of a number of jets, from a minimum of two to maximum of 20, arranged annularly to provide a hollow conical spray. In each individual 'Y', oil is injected into the mixing port, where it mixes with the atomizing fluid (steam or air) admitted through the gas port. The mixing ports are uniformly spaced around the atomizer body at an angle to the nozzle axis (see Figure 1) so that the individual jets of two-phase mixture emanating from the mixing ports rapidly merge to form a hollow conical spray.

The spraying performance (expressed by the mean droplet size) of the Y-jet atomizer is reported to be affected by properties of gas and liquid, injection pressure, and also by the geometric configurations such as the mixing-port size and the intersecting angle between the liquid and gas ports. Mullinger and Chigier (Mullinger & Chigier, 1974) and Prasad (Prasad, 1982) studied the effect of geometric parameters on the mean drop size and suggested the design criteria to generate the fine droplets. Song and Lee (Song & Lee, 1994) conducted the experimental examination, with water and air as test fluids, to study the effect of mixing port length on the Y-jet atomizer's spray performance. They concluded that the mean droplet size decreases and becomes spatially even as the mixing port length is reduced. In a classical study, with water and air as working fluids, Song and Lee (Song & Lee, 1996) studied the atomization mechanism of the gas-liquid mixture flowing through internally mixing twin-fluid Y-jet atomizer by examining both the internal and external nozzle flow patterns. They compared two operational parameters, namely gas-to-liquid mass flow rate ratio (GLR) and liquid-to-gas momentum ratio to describe the internal flow patterns and external drop size distribution. The atomization model of Y-jet atomizer proposed by Mullinger and Chigier (Mullinger & Chigier, 1974), Song and Lee (Song & Lee, 1996) and Andreussi et al. (Andreussi, et al., 1992) is almost the same. The main difference is that the internal atomization mechanism proposed by Song and Lee is subdivided into two parts namely direct collision mode and entrainment/deposition mode.

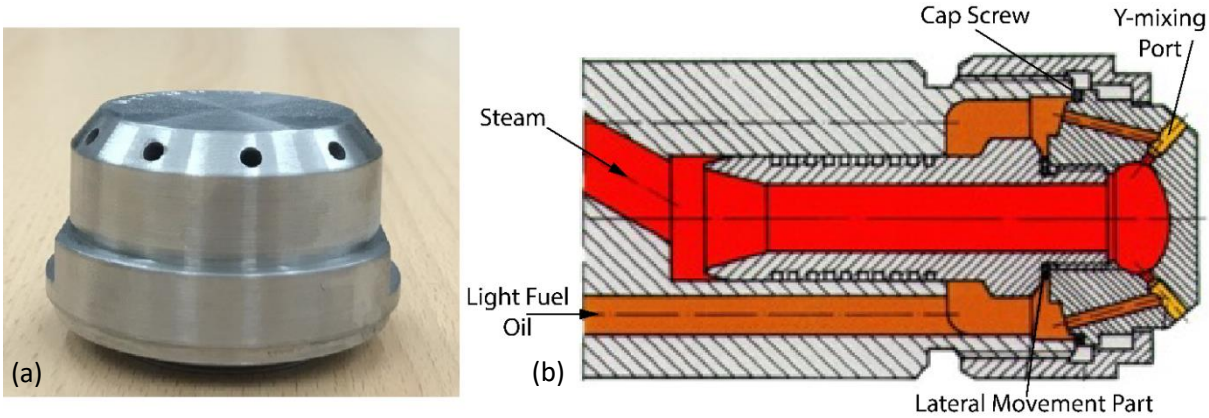

Figure 1 (a) Nozzle head of twin fluid Y-jet atomizer (b) Schematic of internally mixing twin-fluid Y-jet atomizer.

There are few studies predicting the internal flow characteristics, flow rates and energy required for the atomization (Nazeer, et al., 2019), (De Michele, et al., 1991), (Andreussi, et al., 1994), (Andreussi, et al., 1992) and (Song & Lee, 1994). There also exist several studies on the atomization characteristics of twin-fluid Y-jet atomizers (Song & Lee, 1996), (Mullinger & Chigier, 1974), (Neya, et al., 1975), and (Andreussi, et al., 1994); parameters such as atomizer geometry and injection conditions were taken as "input" and the spray performance was considered as "output." However, the effect of internal flow conditions on the atomization characteristics is not reported in detail. The effect of internal flow condition can be understood only by looking into both the internal flow patterns and the atomization mechanism simultaneously. (Neya, et al., 1975), (Andreussi, et al., 1994) and (Song & Lee, 1996) are the only cases paying attention to the effect of internal flow pattern on the atomization. However, the results are restricted to simplified conditions and geometry, and water and air as working fluids.

A broad range of time and length scales are involved in atomization; thus, approximations and modeling of unresolved sub-grid scale phenomena become inevitable in CFD of such multiphase flow phenomena (Li, et al., 2020). The numerical simulation of the liquid spray generation often aims in predicting drop size distribution, spray penetration length and spray cone angle (Zhou, et al., 2019 a) and (Zhou, et al., 2019 b). Since the liquid spends most of its residence time in the form of droplets, simulation methodologies for the dispersed multiphase flow are usually utilized. The two widely

implemented approaches used for the description of the dispersed phase are the Eulerian-Eulerian and Eulerian-Lagrangian.

The Eulerian-Eulerian multiphase approach describes the motion of the dispersed phase by the same means as the continuous phase, i.e. a set of Navier-Stokes equations for the continuity and momentum transport, potentially along with transport equations for energy and other conserved quantities. The gas-liquid interface can be tracked by an additional transport equation such as the widely used VOF method (Hirt & Nichlos, 1981) or similar and early applications to internal nozzle flow and atomization (Arcoumanis, et al., 1999) and (Gavaises & Arcoumanis, 2001). Such methods requires much smaller time steps and much higher mesh resolutions than diffuse interface approaches and Eulerian-Lagrangian methods, as the computational mesh around the phase boundary of each droplet must be refined enough to adequately resolve. The volume displacement is inherently accounted for, which can be important for the dense part of the spray. However, this method is prohibitive in terms of computational expenses and requires large HPC resources.

In Eulerian-Lagrangian multiphase approaches (Jiang, et al., 2010), referred to as Discrete Particle Methods (DPM), the gas/carrier phase is still represented by solving the governing equation of the flow but the liquid phase is represented by a number of discrete computational particles, which are tracked through the domain by solving the particle's equation of motion. Particle tracker use physical properties of individual droplets in order to account for the exchange of mass, momentum and energy etc. with the continuous phase. This approach is relatively inexpensive since it allows the mesh to be coarser than the size of the droplets. However, the gas volume displacement is usually ignored; this may affect the solution's accuracy, hence these so-called dense models have been developed (Tonini, et al., 2008). Furthermore, in the regions where spray does not consist of discrete spherical droplets, special models must be employed to predict the primary breakup of the initial contiguous jet.

ANSYS Fluent provides the capability to combine the above mentioned two approaches through VOF-to-DPM transition mechanism. The initial jet and its primary breakup are predicted using VOF formulations on sufficiently fine mesh, while the resulting dispersed part of the spray is predicted by the DPM. The ELSA model (Vallet, et al., 2001) and (Nykteri, et al., 2020) is another alternative approach that provides a dynamic transition between an Eulerian and a Lagrangian framework in the primary and secondary liquid spray atomization regions, respectively. The hybrid VOF-to-DPM model automatically finds the liquid lumps detached from the liquid core in the VOF solution. It then checks for their eligibility for the VOF-to-DPM model transition against the user specified criteria of the lump size and asphericity. If a liquid lump satisfies the criteria, the liquid lump is removed from VOF solver and converted to a point mass in the Lagrangian formulations. Converting liquid lumps to Lagrangian formulation does not impose volume displacement on the continuous phase VOF flow simulations. In order to circumvent spurious momentum sources, a volume of a gas with the same volume as the liquid lump is created in the VOF simulation to maintain the volume conservation. The hybrid VOF-to-DPM model is validated against the experimental studies to determine the Sauter mean diameter (SMD) drop size distribution for a liquid jet in air cross-flow (Schtze, et al., 2018) and (Sami, et al., 2019) and also the reverse transition mechanism i.e. DPM-to-VOF is reported to agree well with the experimental studies to determine the film formation from the drops (Kumar, et al., 2018).

In the present study, the multiphase flow through the internally mixing twin-fluid Y-jet atomizer is numerically modelled to determine the internal flow behavior and the subsequent atomization mechanism. It is the first numerical study to report the atomization mechanism of the internally mixing twin-fluid Y-jet atomizer. The influence of two dimensionless operating parameters, namely gas-to-liquid mass flow rate ratio and liquid-to-gas momentum ratio are compared; the latter is found to be more appropriate dimensionless parameter to describe the internal flow behavior and the atomization characteristics, as it defines to a large extend the liquid and gas distribution inside the atomizer, which then affects the near-nozzle atomization and the distribution of the formed ligaments and droplets. It should be also mentioned that although more sophisticated atomization

models exist in the literature for the fragmentation of liquids, the applied model has been validated from the author's group for other flow conditions, like for example the secondary break-up of liquid droplets (Stefanitsis, et al., 2019a), (Stefanitsis, et al., 2019b), (Strotos, et al., 2018), (Strotos, et al., 2016a), (Strotos, et al., 2016b) and (Strotos, et al., 2011). For the specific conditions simulated here, the complexity of the flow within the atomizer, it is unfortunate that quantitative experimental data for the atomizing spray that would be needed for quantitative validation of the applied computational models do not exist.

Following, the computational model utilized and the geometry and operating conditions are described, followed by the presentation of the results; these include initially the flow structure inside the atomizer and then its influence on the spray formation; the most important conclusions are summarized at the end.

Numerical Method

VOF

The compressible Navier-Stokes equations are numerically solved using the finite volume approximation; the Volume of Fluid (VOF) technique with Geometric Reconstruction Scheme is employed in ANSYS Fluent with a time step of 10^{-8} to model the gas-liquid interface. The interface is modeled as interpenetrating media; the two phases are sharing same properties while the bulk properties of the individual phase are scaled according to the cell's volume fraction which varies between zero and one.

The corresponding transport equations that consider the volume fraction in the cell, with ρ_q representing the density and $\overrightarrow{V_q}$ the velocity vector of the q^{th} phase, are:

$$\frac{d}{dt}\left(\alpha_q \rho_q\right) + \nabla.\left(\alpha_q \rho_q \overrightarrow{V_q}\right) = 0 \quad (1)$$

The single set of momentum equation is shared among the phases based on mixture properties.

$$\frac{d}{dt}(\rho\vec{V}) + \nabla.(\rho\vec{V}\vec{V}) = -\nabla P + \nabla.\left[\mu\left(\nabla\vec{V} + \nabla\vec{V}^T\right)\right] + \rho\vec{g} + \vec{T}_\sigma \quad (2)$$

175

176 Where density is defined as: $\rho = \sum \alpha_q \rho_q$, viscosity as: $\mu = \sum \mu_q \alpha_q$, and velocity as: $\vec{V} =$

177 $\frac{1}{\rho}\sum_{q=1}^{n} \alpha_q \rho_q \vec{V}_q$ $\vec{T}_\sigma$ is the volumetric force source term arising due to the surface tension. It is

178 modelled by continuum surface force model proposed by Brackbill et al. (Brackbill, et al., 1992). This

179 model treats the surface tension as the pressure jump across the interface. The forces at the surface

180 are expressed as volume forces using the divergence theorem:

$$T_\sigma = \sum_{pairs,p,q} \sigma_{p,q} \frac{\alpha_p \rho_p k_q \nabla\alpha_q + \alpha_q \rho_q k_p \nabla\alpha_p}{\frac{1}{2}(\rho_p + \rho_q)} \quad (3)$$

181

182 The curvature of one surface is negative of other, $k_p = -k_q$ and divergence of the volume fraction is

183 negative of other $\nabla\alpha_p = -\nabla\alpha_q$. This simplifies the equation to:

$$T_\sigma = \sigma_{p,q} \frac{\rho k_p \nabla\alpha_p}{\frac{1}{2}(\rho_p + \rho_q)} \quad (4)$$

184 The total energy of the flow is modelled by following equation.

$$\frac{d}{dt}(\rho E) + \nabla.\left(\vec{V}(\rho E + P)\right) = \nabla.\left(K_{eff}\nabla T + \bar{\bar{\tau}} \cdot \vec{V}\right) \quad (5)$$

185

186 Here K_{eff} is effective thermal conductivity, $\bar{\bar{\tau}}$ is the viscous stress tensor; the energy E and

187 temperature T are mass averaged variables.

$$E = \frac{\sum_{q=1}^{n} \alpha_q \rho_q E_q}{\sum_{q=1}^{n} \alpha_q \rho_q} \quad (6)$$

188

189 E_q is the internal energy of each phase; both phases share the same temperature.

190 Transition

Asphericity is the shape base criterion used by VOF-to-DPM model to identify the liquid lumps which can be converted from resolved liquid using VOF model to particles tracked with the DPM model. Its value is zero for a perfect sphere. Asphericity values of the liquid lumps are determined in two ways, namely calculated from normalized radius standard deviation and radius-surface orthogonality. In the first method, for every facet of the liquid lump surface, the distance between the facet center and the lump center of gravity is calculated and then normalized by the average radius. In the second method, for every facet of the liquid lump surface, a vector from the lump's center of gravity to the center of the lump boundary facet is computed and then used in a dot product with the facet unit normal vector. Only lumps for which the asphericity values calculated from both methods are below the user-specified maximum asphericity values are selected for transition from VOF liquid to DPM particles.

DPM

The trajectory of the discrete phase is predicted by integrating the force balance on the particle. The force balance equation, which is written in a Lagrangian reference frame, equates the particle inertia with the force acting on the particle. It can be written as:

$$\frac{d\vec{V}_{pr}}{dt} = F_D\left(\vec{V} - \vec{V}_{pr}\right) + \frac{\vec{g}(\rho_g - \rho)}{\rho_{pr}} \tag{7}$$

Where $F_D\left(\vec{V} - \vec{V}_{pr}\right) + \frac{\vec{g}(\rho_{pr} - \rho)}{\rho_{pr}}$ is the drag force per unit particle mass and

$$F_D = \frac{18\mu}{\rho_{pr} d_{pr}^2} \frac{C_D Re_r}{24} \tag{8}$$

Here, $\vec{V}$ is the fluid phase velocity, $\vec{V}_{pr}$ is the particle velocity, μ is the molecular viscosity of the fluid, ρ_{pr} is the density and d_{pr} is the diameter of the particle. Re_r is the relative Reynolds number, it is defined as:

$$Re_r = \frac{\rho d_p |\vec{V}_{pr} - \vec{V}|}{\mu} \tag{9}$$

C_D is the drag coefficient; according to Morsi and Alexander model (Morsi & Alexander, 1972), it is defined as:

$$C_D = a_1 + \frac{a_2}{Re} + \frac{a_3}{Re^2} \tag{10}$$

Where a_1, a_2 and a_3 are defined as:

$$a_1, a_2, a_3 = \begin{cases} 0, 24, 0 & 0 < Re < 0.1 \\ 3.690, 22.73, 0.0903 & 0.1 < Re < 1 \\ 1.222, 29.1667, -3.8889 & 1 < Re < 10 \\ 0.6167, 46.50, -116.67 & 10 < Re < 100 \\ 0.3644, 98.33, -2778 & 100 < Re < 1000 \\ 0.357, 148.62, -47500 & 1000 < Re < 5000 \\ 0.46, -490.546, 578700 & 5000 < Re < 10000 \\ 0.5191, -1662.5, 5416700 & Re > 10000 \end{cases} \tag{11}$$

The heat balance to relate particle temperature to convective heat transfer at the droplet/particle surface is modeled by following equation:

$$m_{pr} c_{pr} \frac{dT_{pr}}{dt} = hAr_{pr}\left(T_\infty - T_{pr}\right) \tag{12}$$

where m_{pr} is the mass of the particle, c_{pr} is the heat capacity of the particle, Ar_{rp} is the surface area of the particle, T_∞ is the local temperature of the continuous phase and h is the convective heat transfer coefficient. The convective heat transfer coefficient is evaluated using the correlation of Ranz and Masrshall (Ranz & Marshall, 1952 a) and (Ranz & Marshall, 1952 b) as:

$$\frac{hd_p}{k_\infty} = 2.0 + 0.6 Re_r^{1/2} Pr^{1/3} \tag{13}$$

Here k_∞ is the thermal conductivity and $Pr\ \left(c_p \mu / k_\infty\right)$ is the Prandtl number of the continuous phase

Turbulence Modeling

Scale resolving technique is adopted to resolve larger eddies through Wall Modeled LES (WMLES) Model. As Reynolds number increases and the boundary layer become thinner, the size of important energy bearing eddies decreases. In Large Eddy Simulations (LES), the important energy bearing

eddies must be resolved, thus the cost of maintaining grid resolution becomes prohibitive while much smaller time steps are also required. A promising approach to overcome the Reynolds number scaling limitation of LES is the algebraic Wall-Modeled LES approach. In this model larger eddies are resolved while eddies in thinner near-wall regions; in which the wall distance is much smaller than the boundary-layer thickness but it is still potentially very large in wall units (Piomelli & Balaras, 2002), is modeled with RANS, hence considerably reducing the computational cost. Gaussian filter is applied to filter out eddies based on the length scale Δ (Shur, et al., 2008).

$$\overline{\emptyset}(x,t) = \int_D \emptyset(x',t)G(x,x',\Delta)dx' \tag{14}$$

$$\Delta = min(max(C_w.ds_w; C_w.h_{max}, h_{wn}); h_{max}) \tag{15}$$

h_{max}= maximum edge length, h_{wn}= grid step in wall-normal direction, C_w=0.15, d_w= distance from wall.

After putting the filtered out variables in Navier-Stokes equation and rearranging the terms, it could be expressed as:

$$\frac{(\partial \bar{V}_i)}{\partial t} + \frac{\partial\left(p\bar{V}_i\bar{V}_j\right)}{\partial x_j} = -\frac{\partial \bar{P}}{\partial x_i} + \frac{\partial\left(\tau_{ij} + \tau_{ij}^s\right)}{\partial x_j} \tag{16}$$

This equation could be resolved except of the subgrid-scale stress τ_{ij}^s. It can be expressed by the Boussinesq hypothesis (Hinze, 1975) as:

$$\tau_{ij}^s - \frac{1}{3}\tau_{kk}\delta_{ij} = -2\mu_t S_{ij} \tag{17}$$

The subgrid scale eddy viscosity is modeled with the Smagorinsky SGS model (Smagorinsky, 1963), the van Driest damping (Van Driest, 1956) and mixing length model as:

$$\nu_t = min\left[(\mathrm{k}ds_w)^2, \left(C_{smag}\Delta\right)^2\right]\left[1 - exp[-(y^+/25)^3]\right]|S - \Omega| \tag{18}$$

$C_{smag} = 0.2$ is the Smagorinsky constant, as established by Shur et al (Shur, et al., 1999), Ω= is the vorticity, S is the magnitude of the strain tensor, $\mathrm{k} = 0.41$ is the Von Karman Constant.

Test Case Simulated

Figure 2 depicts the geometry used in the simulations. The figure is not drawn according to scale. The working fluids are superheated steam and light fuel oil. The liquid port has diameter (d_l) 2.1 mm and length (l_l) 30 mm. The gas port has diameter (d_g) $1.6\,mm$ and length (l_g) $4\,mm$. Both the mixing port and the premixed zone has diameter $2.6\,mm$ and lengths $12.4\,mm$ and $5.6\,mm$ respectively. The angle between the fuel port and the mixing port is 42.5°. The pressure and temperature conditions at the inlet of the fuel port are $20^{\circ}C$ and 19 bars, and at the inlet of steam port are $210\,^{\circ}C$ and 11 bars respectively. The density and kinematic viscosity of the light fuel oil are $0.93\ kg/m^3$ and $4{,}1\ mm^2/s$ respectively, while steam is modeled as ideal gas. The condition at the outlet of simulation zone is air at 1 bar and room temperature. The Sauter mean diameters (SMD) of the droplets are measured on each 3 mm slot on the plane A along the Y axis as shown in Figure 2. Plane A is located at the distance of 32 mm from the nozzle orifice. This distance is chosen on the basis of computational affordability. The geometry is meshed in ANSYS Meshing with polyhedral grid. Dynamic solution-adaptive mesh refinement in ANSYS Fluent is used to dynamically adapt the mesh at the gas-liquid interface in the VOF simulations through polyhedral unstructured mesh adaption (PUMA) method. This adaptation travels with the gas-liquid interface and the number of the cells changes with the flow, once liquid lumps are converted into the DPM particles; coarser grid is used to track the particles. This method significantly reduces the mesh count. Three levels of dynamic mesh refinement are used while the minimum cell volume is set to the order of $10^{-16}\ m^3$. The minimum cell volume is chosen based on the droplet size distribution to avoid over-refinement of the grid in order to run the simulations more efficiently. A grid independent study is conducted with a minimum cell volume of $10^{-16}\ m^3$ and $10^{-17}\ m^3$ (equivalent cubic cell size of ~ 5 and $\sim 3\mu m$, respectively). The results are displayed in the appendix I (Figure 9 and Figure 10). It can be seen in Figure 9 that the drop size distribution and in Figure 10 that the average volume fraction of the light fuel oil over one hundred thousand time steps are almost the same for both meshes. Figure 3 shows an instantaneous

picture of numerical grid; it can be seen that the mesh is refined around gas-liquid interface. Mass flow inlet boundary conditions are used for the inlets and pressure outlet boundary condition is used for the outlet. In the first set of the simulations the mass flow rate of the steam is kept constant at $0.00400\ kg/s$ while the mass flow rate of fuel oil is varied from $0.1329\ kg/s$ to $.38\ kg/s$; the corresponding values of steam-to-fuel oil mass flow rate ratios are from 0.01053 to 0.0301 respectively. In the second set of simulations, the mass flow rate of the steam is kept constant at $0.0005\ kg/s$ while the mass flow rate of the fuel oil is varied from $0.005\ kg/s$ to $0.0167\ kg/s$; the corresponding steam-to-fuel oil mass flow rate ratios are from 0.03 to 0.1 respectively. The Reynold numbers for the flow conditions simulated are between 10,000 and 13,000. They are calculated from the following expression:

$$Re = \frac{\rho_{mix,M} V_r d_m}{\mu} \tag{19}$$

Here $\rho_{mix,M}$ is the average mixture density of the gas and liquid at the mixing point, V_r is the relative velocity between gas and liquid phase, and d_m is the mixing port diameter.

The asphericity value for the VOF-to-DPM transition mechanism is initially set to the value of 0.01. As the flow is developed in the mixing port of the atomizer, it is changed to the value of 2.5 to track the droplets and measure its SMD.

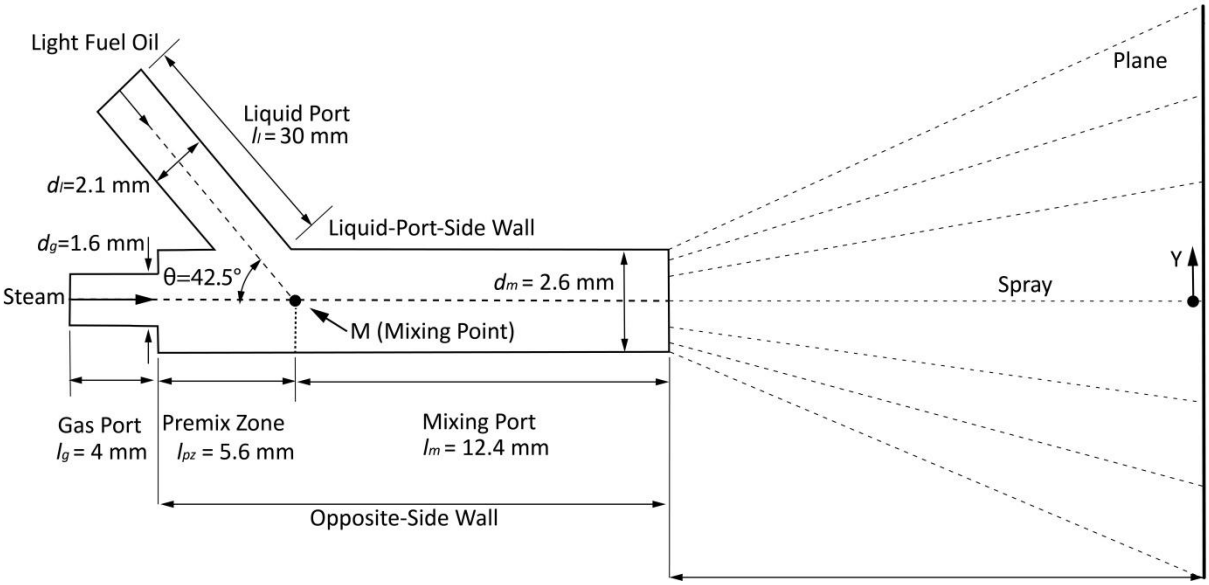

Figure 2: Geometry of twin-fluid Y-jet atomizer used in the simulation and schematic explanation of the subsequent spray formation.

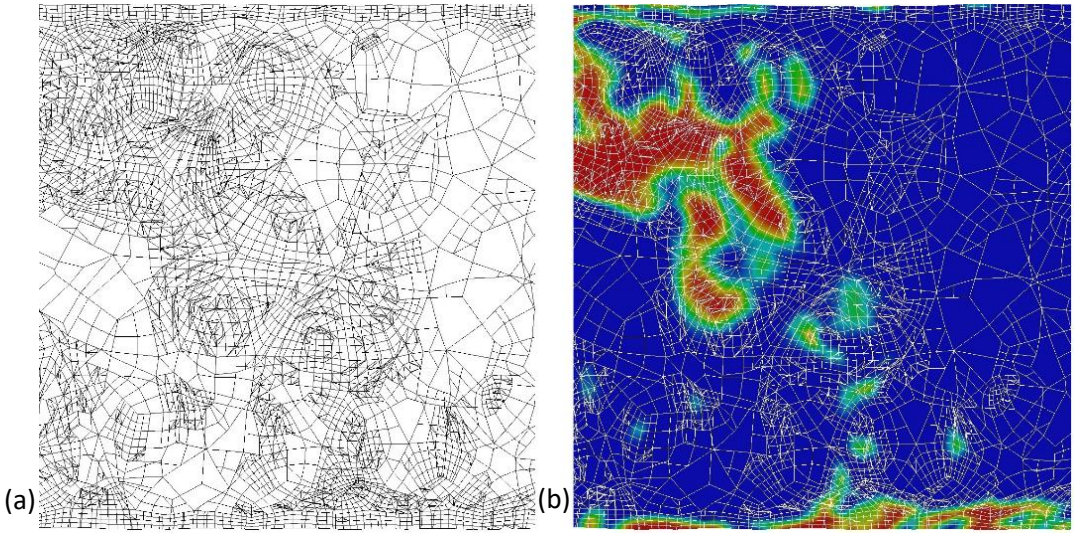

Figure 3 (a) Instantaneous grid (b) Instantaneous grid with super imposed volume fraction of light fuel oil.

Results & Discussion

Visualization of the simulation results has been carried out to analyze the internal flow behavior within the mixing-port of the twin-fluid Y-jet atomizer. Figure 4 show the internal flow patterns within the mixing-port of atomizer for two different steam mass flow rates and various oil mass flow rates. For a reference, a schematic of the mixing-port at the same scale is drawn at the top of Figure 3. The red colour depicts the volume fraction of fuel oil to be 1 while blue colour depicts the volume

fraction of the fuel oil to be zero i.e. the volume fraction of the steam as 1. The instability of the liquid jet emanating from the liquid port into the mixing port is amplified by the impingement of high velocity gas stream; leading to the creation of smaller liquid ligaments and sheets. This phenomenon could be explained by the shear action of the gas stream and by the wave lengths that grow on the surface of the liquid jet/column, which are affected by surface tension, aerodynamic and viscous forces (Dombrowski & Johns, 1963). The high relative velocity of the gas helps the dispersion of the liquid and delays or minimise the chances of droplet coalescence (Pacifico & Yanagihara, 2014).

At first, it can be realized from the contours in the Figure 4 that both M_l and M_g clearly influence the oil film formation within the mixing port. The amount of oil stream crossing the mixing port increases with a decrease of M_g and/or an increase of M_l, and forms a thicker oil film at the opposite side wall. The internal flow pattern far downstream of the mixing point becomes an annular-mist flow with asymmetrical film thickness along the wall of the mixing-port, as characterized by Mullinger and Chigier (Mullinger & Chigier, 1974), Andreussi et al. (Andreussi, et al., 1994), (Andreussi, et al., 1992), Pacifico and Yanagihara (Pacifico & Yanagihara, 2014) Mlkvik et al. (Mlkvik, et al., 2015) and Nazeer et al. (Nazeer, et al., 2019). The rate of direct drop formation within the mixing port is also strongly dependent on both M_g and M_l. That is, the number of drop increases with an increase in M_l and/or M_g (Song & Lee, 1996).

On the same figure, the values of the gas-to-liquid mass flow rate ratio (M_g/M_l) and the liquid-to-gas momentum ratio (φ) are also shown. These parameters are already adopted in the studies (Neya, et al., 1975), (De Michele, et al., 1991), (Andreussi, et al., 1992), (Song & Lee, 1994), (Andreussi, et al., 1994), (Pacifico & Yanagihara, 2014), (Mlkvik, et al., 2015) and (Nazeer, et al., 2019). Here φ is defined as:

$$\varphi = \frac{{G_l}^2 {d_l}^2 \rho_{gM}}{{G_g}^2 {d_m}^2 \rho_l} \sin\theta \tag{20}$$

Where "G" is the mass velocity, "ρ" is the density, "d_m" is the mixing port diameter and "θ" is the angle between liquid and gas ports. The indices "g" and "l" denote the gas and liquid respectively; ρ_{gM} is the density of the steam at the mixing point.

From Figure 4 one can point out that when the gas flow rates are different while M_g/M_l is kept constant (see Figures 4a and 4i), the flow pattern appears to be much different. In fact, when momentum ratios are near to each other, for instance (4a and 4f) and (4h and 4c) flow development looks very similar. Thus, from the above observations, the liquid-to-gas momentum ratio (φ) seems to be a better dimensionless parameter to explain the internal flow pattern than the gas-to-liquid mass flow rate ratio. Song and Lee (Song & Lee, 1996) also reached to the conclusion that momentum ratio is a better parameter to describe the internal flow pattern.

Figure 5 helps to explain the variation in gas and liquid flow patterns within the mixing port of Y-jet nozzle based on the momentum ratio. The contours of the volume fraction of light fuel oil are displayed for the liquid-to-gas momentum ratios of 3.2, 7.3 and 9.4. When the liquid-to-gas momentum ratio is low (say $\varphi < 7$, Figures 4a, 4e, 4f and 4g), most of the liquid forms thick film at liquid-port-side wall of the mixing port. This is because the gas jet momentum dominates and liquid stream cannot penetrate into the mixing-port easily. Due to this, the main stream of the gas tends to be deflected towards the opposite side wall by the liquid film and thus, a large recirculation appears in the premix zone. Hence, a portion of the liquid stream flows in a film shape toward the upstream by recirculating gas. For example the liquid film in the upper left corner of Figures 4b, 4f, 4g and 4i clearly indicates the reverse flow of the liquid film by strong recirculation of the gas. As the main gas stream at the exit of the gas port meets the reverse flow, it disintegrates in to small droplets and flows downstream along the core, as it can be seen in Figure 6. At the same time, as it can be seen in Figures 4a, 4e, 4f and 4g, droplets are also entrained from the main liquid film, flowing downstream.

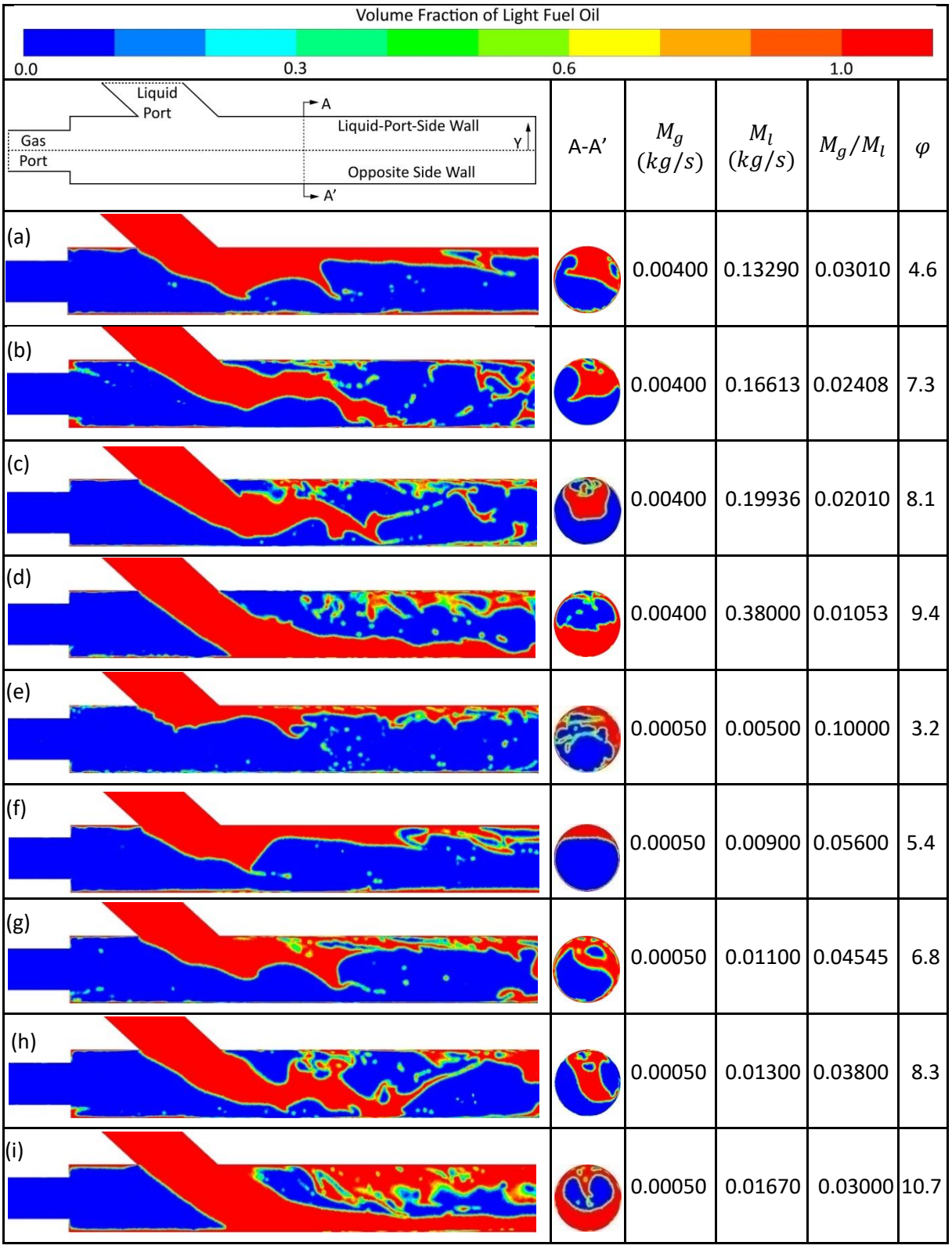

348 Figure 4 Internal flow pattern within the mixing port of internally mixing twin-fluid Y-jet atomizer at the flow time of 0.001 s for the liquid-to-gas momentum ratios of (a) 4.6, (b) 7.3, (c) 8.1, (d) 9.4, (e) 3.2, (f) 5.4, (g) 6.8, (h) 8.3 and (i) 10.7.

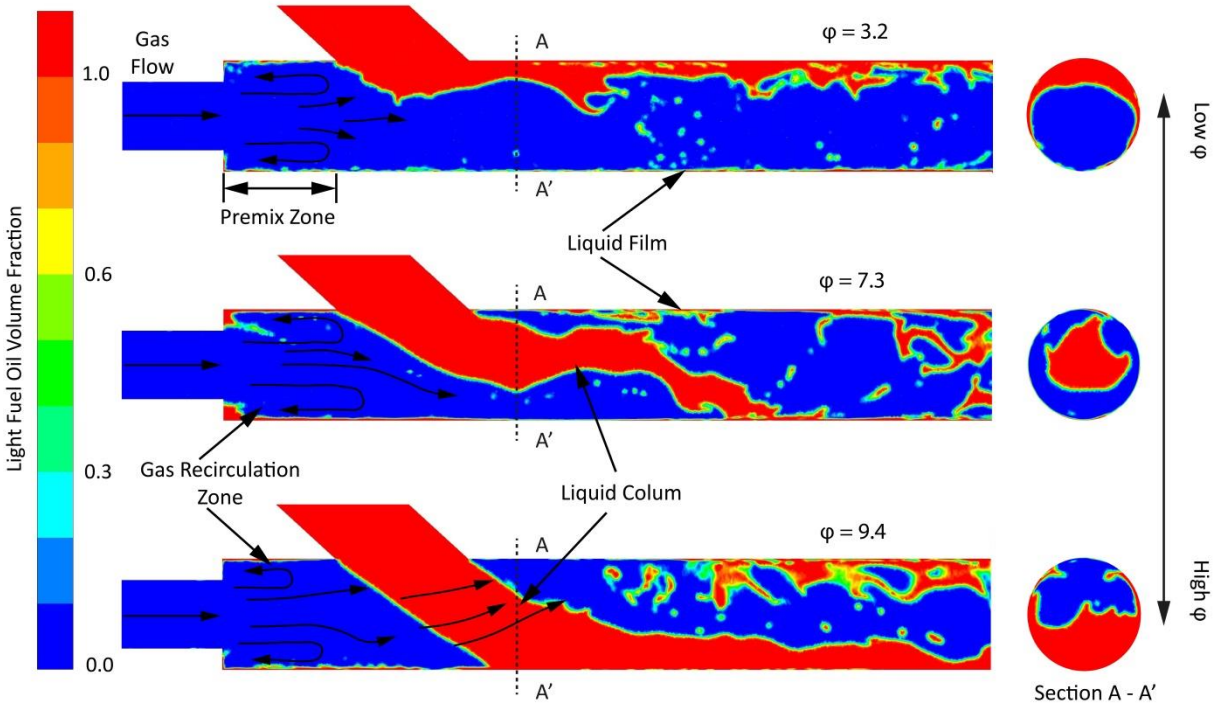

Figure 5 Illustration of internal flow pattern based on liquid-to-gas momentum ratio.

When the liquid-to-gas momentum ratio increases (for $7 < \varphi < 9$, Figures 4b, 4c and 4h), the liquid jet penetrates into the center of the mixing port and starts to blocking the path of the flowing gas ensuing from the gas port; this leads to deflection of the gas stream towards the opposite side wall. This is denoted as blockage effect (Mullinger & Chigier, 1974). Thus, a substantial amount of liquid film at the opposite side is entrained into the gas core by the highly deflected gas stream while the rate of the entertainment increases with the amount of gas stream deflection. The number of droplets formed around the mixing point from the liquid column increases with increasing penetration depth of liquid, since the interfacial area between the gas and liquid increases. The liquid jet in this regime is unstable and gradually breaks up as a result of imbalance between surface forces, velocity fluctuations, pressure fluctuations and steep velocity gradients. This leads to temporally fluctuating liquid sheet/film formation within in the mixing-port, just before the orifice exit (Figures 4b and 4h).

As the liquid-to-gas momentum ratio increases further ($\varphi > 9$, Figures 4d and 4i), part of the liquid jet reaches the opposite wall and the liquid film thickness at both sides of the mixing port becomes similar in thickness. If the liquid-to-gas momentum ratio increases further, the liquid jet completely reaches the opposite side wall and the film thickness at the opposite side wall becomes thicker than the liquid-port-side wall, as can be seen in the Figure 4d. With this condition, the blockage effect becomes more prominent because the gas stream has to flow around the liquid jet crossing the mixing point. Due to the high shear of the gas flow, thin sheets of the liquid are extracted from the liquid jet around the mixing point (liquid-port-side wall Figures 4d and 4i). These sheets are further

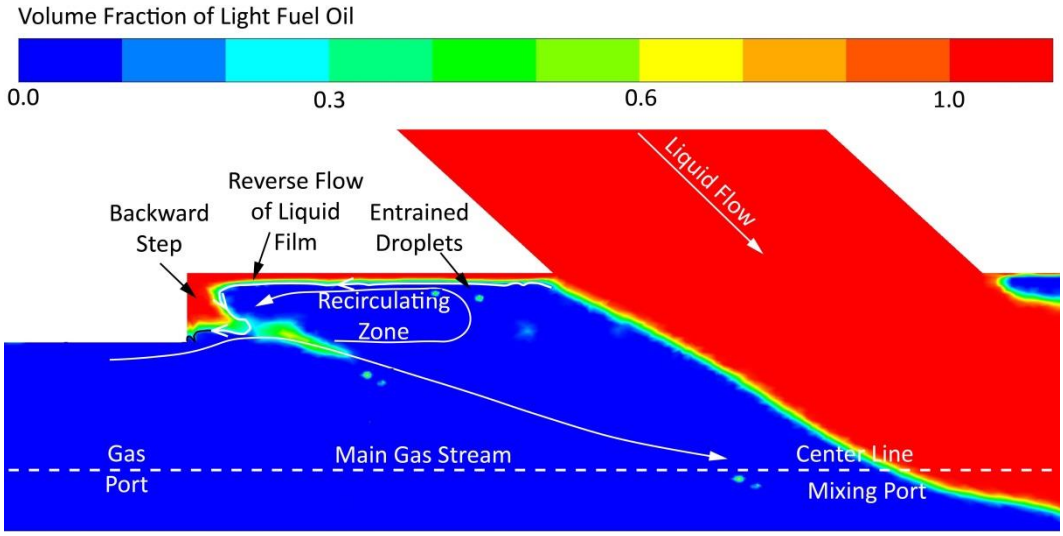

Figure 6 Illustration of the recirculating flow in the premix zone of the mixing port of the atomizer.

broken down into smaller droplets in the downstream flow. The quantity of these liquid sheet formations increases with the deeper penetration of the liquid jet or with greater gas flow rate.

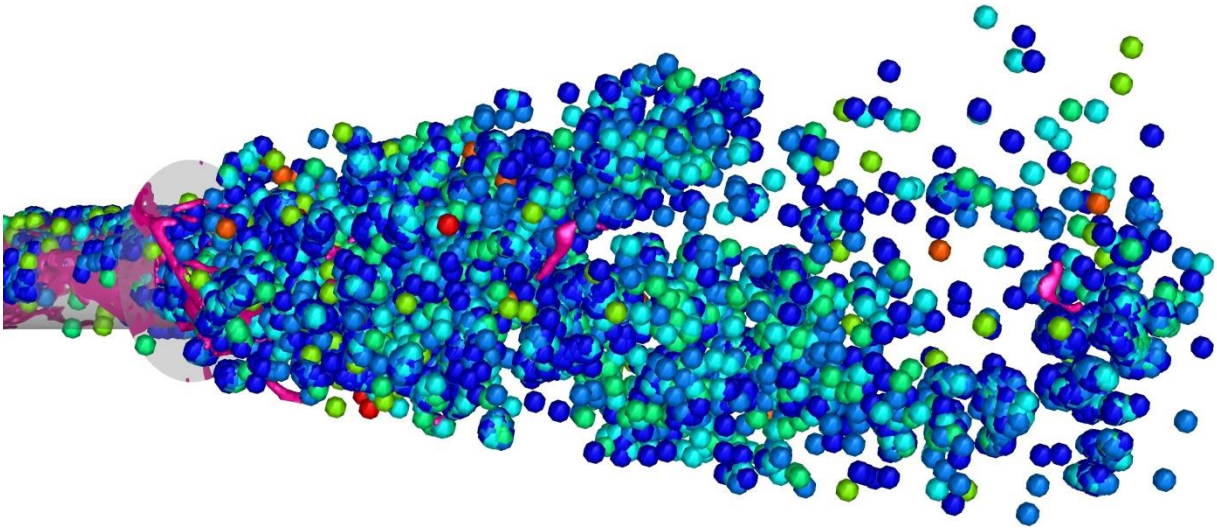

Figure 7 Spray formation by internally mixing twin-fluid Y-jet atomizer at the flow time of 0.0006 s for the liquid-to-gas momentum ratio of 7.3. The magenta colored blobs and ligaments represent the liquid resolved by VOF formulations and spherical particle represents the liquid droplets tracked by DPM model.

Figure 7 shows the spray formation process of internally mixing twin-fluid Y-jet atomizer. The magenta colored blobs and ligaments depict the resolved liquid by the VOF method. Once the specified criteria of asphericity are satisfied, the resolved liquid is turned into discrete droplets, as represented by the spherical particles in Figure 7. Figure 8 shows the Sauter Mean Diameter (SMD) drop size distribution for various liquid-to-gas momentum ratios measured on the plane A along the Y axis as indicated in Figure 2. The droplet size distribution is strongly affected by the internal flow pattern and the initial atomization within the mixing port of the nozzle, as explained earlier. That is, the small droplets at the center are forming from the core flow within the mixing port of the atomizer, whereas the larger droplets at both sides are forming from the annular liquid film present on the walls of the mixing port. It can be also noticed that as the momentum ratio increases, the peak value of the Sauter Mean Diameter in the positive Y axis decreases, indicating that the liquid film thickness at the liquid-port-side wall of the mixing port decreases, due to easier penetration of the liquid column into the gas stream. When the momentum ratio is less than 5.4 (Figures 8a, 8b and 8c), the values of SMD in the negative Y axis changes slightly with the increasing momentum ratios. This is because the liquid column does not have enough momentum to reach the opposite side wall. However, as the liquid-to-gas momentum ratio increases further than that, the values of SMD in the

394 negative Y axis become sufficiently large and the distribution becomes somewhat symmetrical
395 (Figure 8d). If φ increases further, the momentum of the liquid column dominates and hence the
396 values of SMD in the negative Y axis become larger than the values in positive Y axis; the curve again
397 shows asymmetrical shapes. At extremely high values of momentum ratio (Figure 8h), a sudden
398 decrease in the values of SMD in the positive Y axis is observed. This is due to the shear-induced
399 breakup caused by the increased blockage effect (Figure 4h). These distributions agree well with the
400 film thickness variation within the mixing port measured by Andreussi et al. (Andreussi, et al., 1994)
401 and the drop size distribution measured by (Song & Lee, 1996).
402
403
404
405
406
407
408
409
410
411
412
413
414
415
416
417
418
419

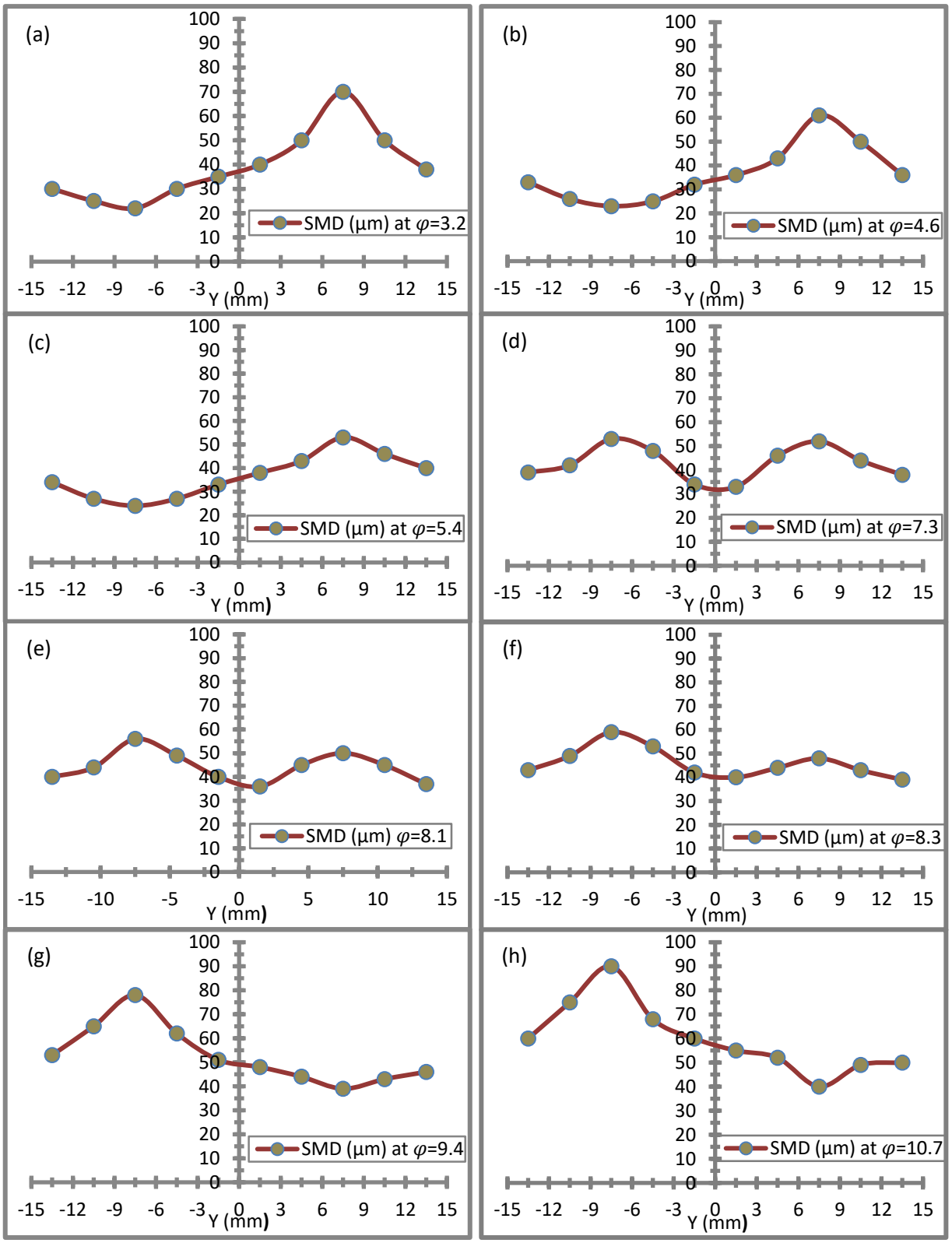

Figure 8 Sauter mean diameter drop size distribution for the liquid-to-gas momentum ratios of (a) 3.2, (b) 4.6, (c) 5.4, (d) 7.3, (e) 8.1, (f) 8.3, (g) 9.4 and (h) 10.7.

Conclusion

Simulation results have been presented for the internal flow behavior and the atomization mechanism of internally mixing twin-fluid Y-jet atomizers. Working fluids were super-heated steam and light fuel oil. The multiphase flow was modeled by hybrid Eulerian-Eulerian and Eulerian-Lagrangian approach through VOF-to-DPM transition mechanism. Adaptive mesh refinement was used to resolve the gas-liquid interface on the fine mesh required by the VOF formulations. When the criteria of asphericity were satisfied, discrete droplets were tracked on the coarser mesh through DPM model. A hybrid RANS and LES technique, i.e. WMLES (wall modeled large eddy simulations) was used to resolve the larger eddies with LES formulations, while smaller eddies were modeled with the Prandtl length model. Two dimensionless parameters namely, gas-to-liquid mass flow rate ratio and the liquid-to-gas momentum ratio have been investigated; the latter is considered to be a more representative dimensionless parameter to describe the internal flow behavior and spray characteristics. The variation in the internal flow pattern, characterized by the penetration of the liquid column into the gas core and the film flow within the mixing port could be effectively explained by the liquid-to-gas momentum ratio. The simulations have confirmed that variation in the circumferential liquid film thickness within the mixing port coincides well with the spatial distribution of the droplets outside the atomizer. Moreover, the variation in the droplet SMD distribution over the Y direction as the function of the liquid-to-gas momentum ratio, agrees well with the mean film thickness and drop size distribution reported previously in the open literature, except for the sharp decrease in the SMD in the positive Y direction at extremely high liquid-to-gas momentum ratios.

Data Availability Statement

ANSYS Fluent case and data files of the simulations that support the findings of this study are available from the corresponding author upon reasonable request.

Acknowledgements

The project has received funding from European Union Horizon-2020 Research and Innovation MSCA-ITN Programme with acronym HAOS: Grant Agreement No. 675676.

References

Andreussi, P. et al., 1994. *Measurement of Film Thickness within a Y-Jet Atomizer.* s.l., International conference on liquid atomization and spray systems, pp. 632-639.

Andreussi, P., Tognotti, L., Michele, G. D. & Graziadio, M., 1992. Design and Characterization of Twin-Fluid Y-Jet Atomizers. *Atomization and Sprays,* Volume 2, pp. 45-59.

Arcoumanis, C., Gavaises, M., Argueyrolles, B. & Galzin, F., 1999. Modeling of Pressure-Swirl Atomizers for GDI Engines. *Transactions Journal of Engines, SAE Paper,* 108(3), pp. 516-532.

Barreras, F., Lozano, A., Ferreira, G. & Lincheta, 2008. *The effect on the inner flow on the performance of a twin-fluid nozzle with an iternal mixing chamber.* Como Lake, European Conference on Liquid Atomization and Spray Systems.

Barreras, F., Lozano, A., Ferreira, G. & Lincheta, E., 2006. *Study of the Internal Flow Condition on the Behavior of Twin-Fluid Nozzle with Internal Mixing Chamber.* Kyoto, International Conference on Liquid Atomization and Spray Systems.

Brackbill, J. U., Kothe, D. B. & Zemach, C., 1992. A continum method for modeling surface tension.. *Journal of Computational Physics,* 100(2), pp. 335-354.

Buckner, H. N., Sojka, P. E. & Lefebvre, A. H., 1990a. Effervescent atomization of coal-water slurries. *ASME publication,* Volume 30, pp. 105-108.

Buckner, H. N., Sojka, P. E. & Lefebvre, A. H., 1990b. *Effervescent atomization of non-Newtonian single phase liquid.* Hartford, Connecticut, Proceedings of the fourth Annual Conference on Atomization and Sprays.

De Michele, G., Graziadio, M., Morelli, F. & Novelli, G., 1991. *Characterization of the spray structure of a large scale H.F.O. Atomizer.* Gaithersburg, Proceedings of ICLASS.

Dombrowski, N. & Johns, W. R., 1963. The aerodynamic instability and disintegration of viscous liquid sheets. *Chemical Engineering Science,* 18(3), pp. 203-214.

Gavaises, M. & Arcoumanis, C., 2001. Modelling of sprays from high-pressure swirl atomizers. *International Journal of Engine Reserach,* 2(2), pp. 95-117.

Hinze, J. O., 1975. *Turbulence.* New York: McGraw-Hill Publishing Co..

Hirt, C. W. & Nichlos, B. D., 1981. Volume of fluid (VOF) method for the dynamics of free boundaries. *Journal of Computational Physics,* 39(1), pp. 201-225.

Inamura, T. et al., 2019. Effects of prefilmer edge thickness on spray characteristics in prefilming airblast atomization. *International Journal of Multiphase Flow,* Volume 121.

Jiang, X., Siamas, G. A., Jagus, K. & Karayiannis, T. G., 2010. Physical modelling and advanced simulations of gas-liquid two-phase jet flows in atomization and sprays. *Progress in Energy and Combustion Science,* Volume 36, pp. 131-167.

Kufferath, A., Wende, B. & Leuckel, W., 1999. Influence of liquid flow condtions on spray characteristics of internal-mixing twin-fluid atomizers. *International journal of heat and fluid flow,* Volume 20, pp. 513-519.

Kumar, V. et al., 2018. *A hybrid approach for modeling fully resolved liquid film formation by converting lagrangian particles to eulerian VOF structures.* Chicago, International Conference on Liquid Atomization and Sprays Systems.

Lefebrve, A. H., 1992. Twin-Fluid Atomization: Factors Influencing Mean Drop Size. *Atomization and Sprays,* Volume 2, pp. 101-119.

Lefebvre, A. H., 1980. Airblast Atomization. *Progress in Energy and Combustion Sciences ,* Volume 6, pp. 223-261.

Li, H., Rutland, C. J., Perez, F. E. H. & Im, G. H., 2020. Large-eddy spray simulation under direct-injection spark-ignition engine-like conditions with an integrated atomization/breakup model. *International Journal of Engine Research.*

Li, Z. et al., 2012. Mixing and atomization characteristics in an internal-mixing twin-fluid atomizer. *Fuel,* Volume 97, pp. 306-314.

Mlkvik, M. et al., 2015. Twin-Fluid atomization of viscous liquids: The Effect of atomizer construction on breakup process, spray stability and droplet size. *International Journal of Multiphase,* Volume 77, pp. 19-32.

Morsi, S. A. & Alexander, A. J., 1972. An investigation of Particle Trajectories in Two-Phase Flow Systems. *Journal of Fluid Mechanics,* 55(2), pp. 193-208.

Mullinger, P. & Chigier, N., 1974. The Design and Performance of Internal Mixing Multijet Twin Fluid Atomizers. *Journal of the institute fuel,* Volume 47, pp. 251-261.

Nazeer, Y. H., Ehmann, M., Koukouvinis, P. & Gavaises, M., 2019. The Influence of Geometrical and Operational Parameters on Internal Flow Characteristics of Internally Mixing Twin-Fluid Y-Jet Atomizers. *Atomizations & Sprays,* 59(5), pp. 403-428.

Neya, K., Sato, S. & Hatopri, K., 1975. Study of y-jet Twin Flid Atomizer. *Ship Reserach Institute ,* 12(1), pp. 1-19.

Nykteri, G. et al., 2020. A Σ-ϒ two-fluid model with dynamic local topology detection: Application to high-speed droplet impact. *Journal of Computational Physics,* Volume 408.

Okabe, T. et al., 2019. Time-dependent breakup length of liquid sheet in prefilming type of airblast atomizer. *Atomization & Sprays,* 29(1), pp. 289-303.

Pacifico, A. L. & Yanagihara, J. I., 2014. The influence of geometrical and operational parametrs on Y-jet atomizers performance. *Journal of Brazilian Society of Mechanical Science and Engineering,* Volume 36, pp. 13-32.

Piomelli, U. & Balaras, E., 2002. Wall-layer Models for Large-Eddy Simulations. *Annual Review of Fluid Mechanics ,* Volume 34, pp. 349-374.

Prasad, K. S. L., 1982. *Characterization of Air Blast Atomizers.* madison wisconsin, International Conference on Liquid Atomization and Spray Systems.

Ranz, W. E. & Marshall, W. R., 1952 a. Evaporation from drops, Part 1. *Chemical Engineering Progress,* 48(3), pp. 141-146.

Ranz, W. E. & Marshall, W. R., 1952 b. Evaporation from Drops Part 1 and Part 2. *Chemical Engineering Progress,* 48(4), pp. 173-180.

Roesler, T. C. & Lefebvre, A. H., 1989. Studies on aerated-liquid atomization. *International journal of turbojet engines,* Volume 6, pp. 221-230.

Roudini, M. & Wozniak, G., 2018. Experimental Investigation of Spray Characteristics of Pre-Filming Air-blast Atomizers. *Journal of Applied Fluid Mechanics,* 11(6), pp. 1455-1469.

Sami, M., Schuetze, P., Hutcheson, P. & Aguado, P., 2019. *Best Practices in the numerical modelling of liquid atomization processes.* Tempe, Arizona, ILASS-Americas 30th Annual Conference on Liquid Atomization and Spray System.

Schtze, J. et al., 2018. *A multimodel hybrid approach for the numerical simulation of fluid phase dispersion process.* Chicago, International Conference on Liquid Atomization and Sprays Systems.

Shur, M. L., Spalart, P. R., Strelets, M. K. & Travin, A. K., 2008. A hybrid RANS-LES approach with delayed-DES and wall-modelled LES capabilities. *International Journal of Heat and Fluid Flow,* Volume 29, pp. 1638-1649.

Shur, M., Strelets, P., Spalart, M. & Travin, A., 1999. Detached-eddy simulation of an airfoil at high angle of attack. *Engineering Turbulence Modeling and Measurements,* Volume 4, pp. 669-678.

Smagorinsky, J., 1963. General Circulation Experiments with the Primitive Equations. *Monthly Weather Review,* Volume 91, pp. 99-165.

Song, S. H. & Lee, S. Y., 1996. Study of Atomization Mechanism of Gas/Liquid Mixtures Flowing Through Y-Jet Atomizers. *Atomization and Sprays,* Volume 6, pp. 193-209.

Song, S. & Lee, S., 1994. *An Examination of Spraying Performance of Y-Jet Atomizers- Effect of Mixing Port Length.* Rouen, International Conference on Liquid Atomization and Spray Systems.

Sovani, S. D., Sojka, P. E. & Lefebvre, A. H., 2001. Effervescent Atomization. *Progress in Energy and Combustion Sciences,* Volume 27, pp. 483-521.

Stefanitsis, D. et al., 2019b. Numerical investigation of the aerodynamic breakup of droplets in tandem. *International Journal of Multiphase Flow,* Volume 113, pp. 289-303.

Stefanitsis, D., Strotos, G., Nikolopoulos, N. & Gavaises, M., 2019a. Numerical investigation of the aerodynamic breakup of a parallel moving droplet cluster. *International Journal of Multiphase Flow,* Volume 121.

Strotos, G. et al., 2011. Non-dimensionalisation parameters for predicting the cooling effectiveness of droplets impinging on moderate temperature solid surfaces. *International Journal of Thermal Sciences,* Volume 50, pp. 698-711.

Strotos, G., Malgarinos, I., Nikolopoulos, N. & Gavaises, M., 2016a. Aerodynamic breakup of an n-decane droplet in a high temperature gas environment. *FUEL,* Volume 185, pp. 370-380.

Strotos, G., Malgarinos, I., Nikolopoulos, N. & Gavaises, M., 2016b. Predicting droplet deformation and breakup for moderate Weber numbers. *International Journal of Multiphase Flow,* Volume 85, pp. 96-109.

Strotos, G. et al., 2018. Determination of the aerodynamic droplet breakup boundaries based on a total force approach. *International Journal of Heat and Fluid Flow,* Volume 69, pp. 164-173.

Tonini, S., Gavaises, M. & Theodorakakos, A., 2008. Modelling of high-presure dense diesel sprays with adaptive local grid refinement. *International journal of Heat and Fluid Flows,* Volume 29, pp. 427-448.

Vallet, A., Burluka, A. A. & Borghi, R., 2001. Development of a Eulerian model for the 1168 "atomization" of a liquid jet. *Atomization and Sprays,* 11(6).

Van Driest, E. R., 1956. On Turbulent flow near a wall. *Journal of Aeronautical Sciences,* Volume 23, pp. 1007-1011.

Zhou, X., Li, T. & Lai, Z., 2019 b. Similarity of split-injected fuel sprays for different size diesel engines. *International Journal of Engine Research.*

Zhou, X., li, T., Wei, Y. & Wang, N., 2019 a. Scaling liquid penetration in evaporating sprays for different size diesel engines. *International Journal of Engine Research.*

Appendix I. Grid Independent Study

A grid independence study was conducted to check whether the drop size distribution measured along the Y axis on the plane A change with the mesh. Two different dynamic solution-adaptive mesh refinements were used through PUMA method. Mesh "I" has three levels of dynamic mesh refinement and minimum cell volume of $10^{-16}\ m^3$, while Mesh "II" has three levels of dynamic mesh refinement and minimum cell volume of $10^{-17}\ m^3$. Average SMD distribution for the momentum rations (φ) 3.2, 7.3 and 9.4 for one hundred thousand time steps are shown in the Figure 9(a), Figure 9(b) and Figure 9(c) respectively. The drop size distribution for both the meshes is almost the same.

Figure 10 shows the contour of the average volume fraction of the light fuel oil within the nozzle over one hundred thousand time steps for the Mesh "I" and Mesh "II" for the momentum rations (φ) of 3.2, 7.3 and 9.4. The average volume fraction for both the meshes for the momentum ratios of 3.2 (figure a & b), 7.3 (figure c & d) and 9.4 (figure e & f) are almost the same.

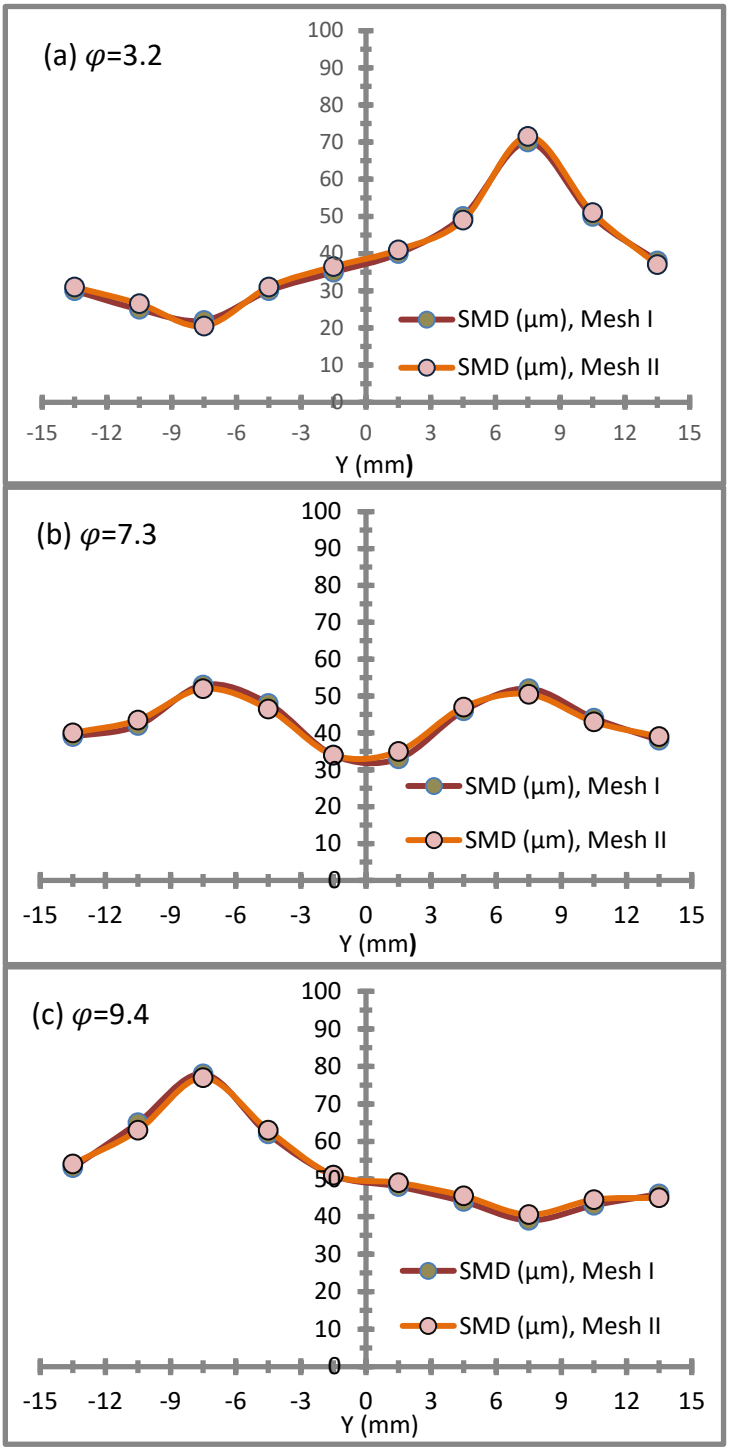

Figure 9 SMD drop size distribution for MESH I and MESH II for the liquid-to-gas momentum ratios of (a) 3.2, (b) 7.3, and (c) 9.4.

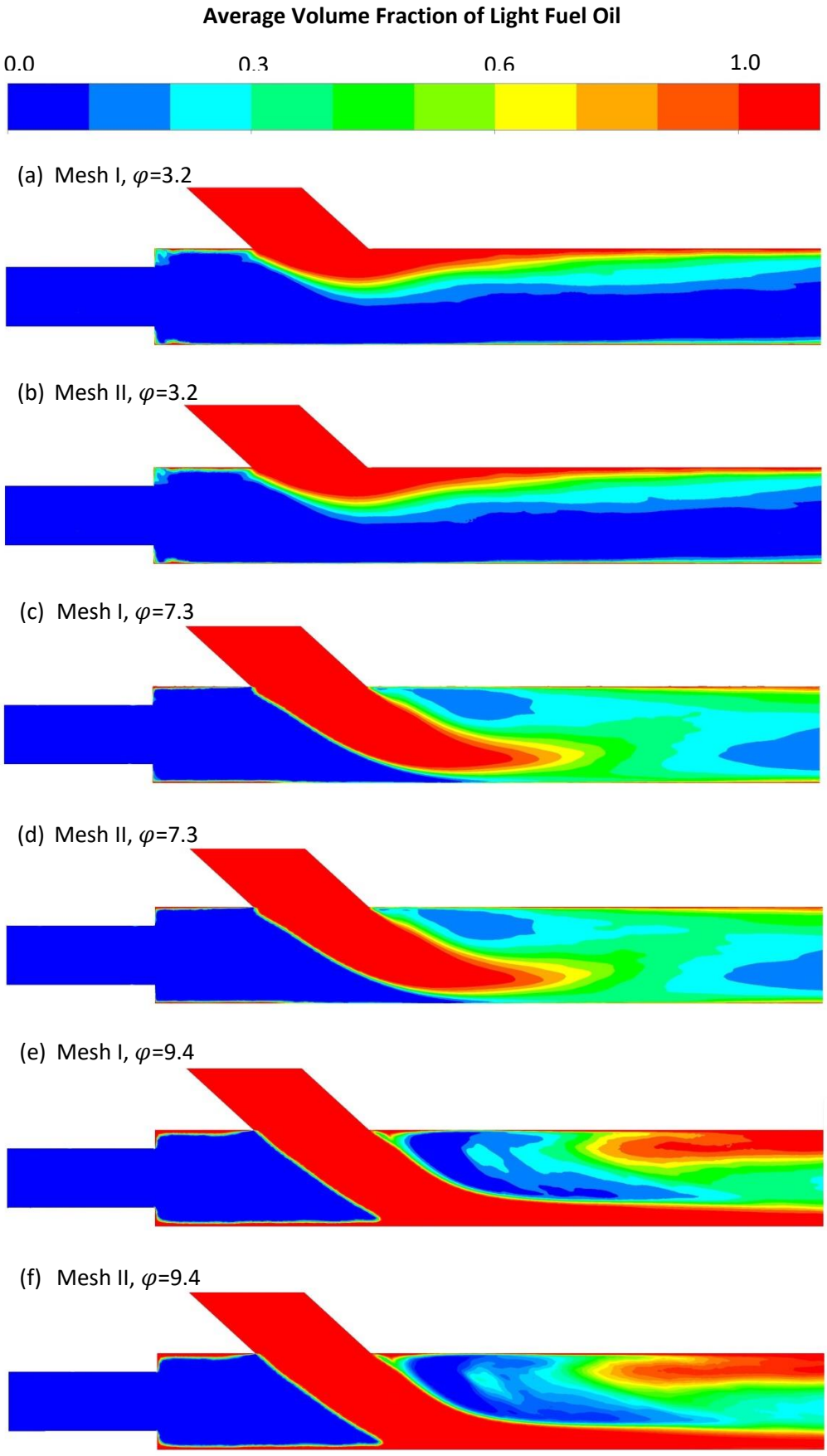

Figure 10 Average volume fraction of light fuel oil over one hundred time steps for liquid-to-gas momentum ratios of 3.2 (a) Mesh 'I' (b) Mesh 'II', 7.3 (c) Mesh 'I' (d) Mesh 'II' and 9.4 (e) Mesh 'I' (f) Mesh 'II'.

Appendix II. Asphericity Independent Study

Figure 11 shows the contour of the average volume fraction of the light fuel oil within the nozzle over one hundred thousand time steps for asphericity of 0.01 and 2.5 for the momentum ratio (φ) of 2.8. The average volume fraction for both the asphericities (figure a & b) are almost the same.

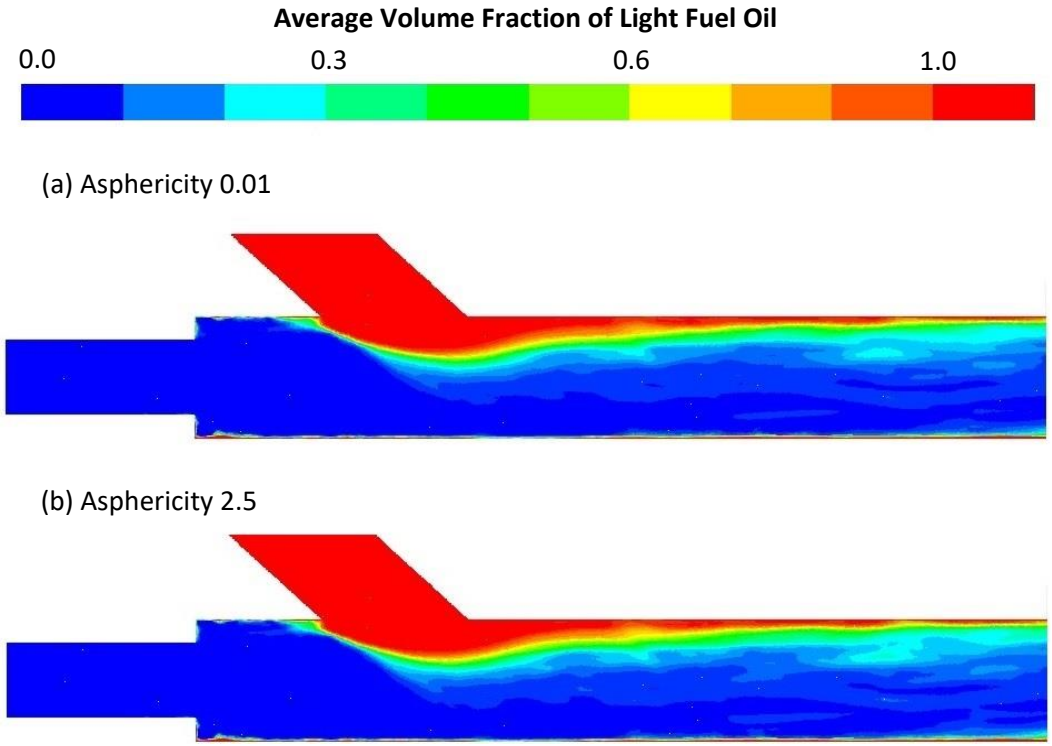

Figure 11 Average volume fraction of light fuel oil over one hundred time steps for asphericity ratios of (a) 0.01 and (b) 2.5 for the liquid-to-gas momentum ratio of 2.8.